Materials Advances

ROYAL SOCIETY OF CHEMISTRY

PAPER

View Article Online
View Journal | View Issue

Cite this: *Mater. Adv.*, 2025, 6, 992

Evaluating nitrogen-doping and elimination effect in peanut shell-derived composites for improving microwave absorption using PMMA as a matrix†

Haniyeh Dogari,[a] Niloofar Salimi-Turkamani,[a] Hossein Ghafuri *[a] and Reza Peymanfar*[bcd]

Received 6th September 2024,
Accepted 4th November 2024

DOI: 10.1039/d4ma00905c

rsc.li/materials-advances

Humans are surrounded by harmful non-visible electromagnetic (EM) waves. Application and production of microwaves have become integral to technology, but it is essential to mitigate their adverse effects while maintaining accessibility to devices. In this study, engineered nitrogen-doping and etching were employed using urea, ball milling, KOH, and reflux treatments to develop optimized microwave-absorbing and shielding composites. Peanut shells were selected as a sustainable carbon source, and nitrogen-doping was enhanced by urea as a dopant, while nitrogen elimination was conducted using HCl and $NaNO_2$. Additionally, polymethyl methacrylate (PMMA) was utilized as a polymeric matrix, fabricated *via in situ* polymerization to create microwave-absorbing composites. The total shielding performance ($SE_T = SE_A + SE_R$), absorption shielding value (SE_A), and reflection shielding parameter (SER) were evaluated. The pyrolized, KOH-refluxed, and nitrogen-doped PMMA composite achieved a reflection loss (RL) of −81.34 dB at 25.61 GHz, with an efficient bandwidth (EBW) of 8.50 GHz (RL ≤ −20 dB) at a thickness of 0.55 mm. Nitrogen elimination led to a maximum RL of −92.38 dB at 23.32 GHz, covering the entire K-band (RL ≤ −20 dB) with a narrow thickness of 0.60 mm. Both samples camouflaged the K-band (RL ≤ −10 dB) at thicknesses between 0.40 and 0.85 mm. Our innovative nitrogen-doping and defect engineering resulted in exceptional microwave absorption and moderate shielding of EM waves, paving the way for practical applications in affordable and sustainable materials.

1. Introduction

Along with water pollution, air pollution, and sound pollution, electromagnetic (EM) pollution menaces human health and the environment.[1–14] Therefore, researchers have focused on microwave-absorbing (MA_s) materials to preserve humans from this type of pollution.[15,16] In recent years, the K-band (18–26 GHz) has emerged as a critical frequency range for various applications, including satellite communications, radar systems, and wireless technologies, such as 5G. Given the increasing prevalence of devices operating in this frequency range, the demand for efficient MA_s materials has become more pronounced. Materials capable of effectively attenuating EM waves within the K-band are essential for mitigating EM interference and reducing the potential health risks associated with EM pollution. Therefore, the development of MA_s materials that perform well in the K-band is of paramount importance for both technological advancement and environmental protection.[17–19] Significant research progress has been made in developing materials with high-performance EM wave absorption and shielding capabilities.[20] Shielding materials have protective properties such as absorption and reflection and, in addition, by increasing the shielding effectiveness, reflection will become stronger.[21] Recent studies have highlighted that advanced designs and modification in composition ameliorate EMI shielding through absorption, reflection, and conductivity mechanisms.[20] MA_s materials can have an innovative architecture with flexibility, low density, high-temperature resistance, lightweight, wide absorption range, and be thin.[22–32] Operation of microwave absorption involves three key mechanisms: reflection, transmission, and absorption.[33] If EM waves encounter absorbing materials, part of the incident energy is reflected back, while some is transmitted through the material.[34] The remaining energy is absorbed by the material, where its dielectric and magnetic properties have crucial roles.[35] This absorbed energy is then transformed into heat, thereby reducing the intensity of the

[a] *Catalysts and Organic Synthesis Research Laboratory, Department of Chemistry, Iran University of Science and Technology, 16846-13114 Tehran, Iran. E-mail: haniyedogari@gmail.com, Niloofarsalimi6@gmail.com, ghafuri@iust.ac.ir*
[b] *Department of Chemical Engineering, Energy Institute of Higher Education, Saveh, Iran. E-mail: reza_peymanfar@alumni.iust.ac.ir*
[c] *Iranian Society of Philosophers, Department of Science, Tehran, Iran*
[d] *Peykareh Enterprise Development CO, Tehran, Iran*

† Electronic supplementary information (ESI) available. See DOI: https://doi.org/10.1039/d4ma00905c

EM waves that pass through the material.[36] Recent research has highlighted the diverse applications of EM wave absorbers in sectors such as stealth technologies, telecommunications, and the automotive industry, where reducing EM interference is essential for performance and safety.[37] These materials also exhibit the ability to convert absorbed microwave energy into heat, making them promising candidates for thermal energy-storage systems.[38] This dual functionality enhances operational efficiency and paves the way for sustainable energy solutions.[38] The heteroatoms existing in the chemical nature, accessibility, affordability, morphology, and specific surface area are the pivotal parameters leading to the selection of biomass sources. Biomass from *Typha orientalis*, peat moss, and almond shells is a perfect applicant for absorbing microwaves.[31,39–42] The main reason for using such biomass in microwave-absorbing systems is the high dielectric feature, lightweight structure, and superior microwave absorption.[29,43–48]

Pyrolysis of carbon-based materials can serve as a promising scenario for activating carbon by a reduction process, and strengthening electrical conductivity by establishing and improving π and n-to-π* charge transitions.[49,50] Pure carbon materials have an orderly lattice of carbon, which can supply effective migrations of free electrons.[5,48,51–57] Biomass-derived structures provide conductive and polarization loss due to their conjugated structure, meanwhile suffering from impedance mismatching and poor permeability.[50,58–63] To overcome these shortcomings, doping and ornamenting by magnetic and other dielectric components have been performed.[2,55,59,62,64–67] The interaction between nitrogen and carbon within samples significantly enhances interfacial polarization, a key mechanism for effective microwave absorption.[68] Through nitrogen doping, nitrogen-rich regions and defects can be introduced into the carbon structure, creating localized dipoles that polarize under an external EM field and exchange resonances.[69] This response improves dielectric behavior and enhances energy dissipation, contributing to efficient absorption of EM waves.[70] *In situ*-synthesized nitride and carbide-based structures have large surface areas, which provide numerous active sites that enable the accumulation and redistribution of charge.[68] These extensive surface areas and the stability of these materials support enhanced polarization effects, improving the performance of the material in EM applications.[68]

The lattice of pure carbon would be destroyed by the decay of heteroatom atoms, resulting in a large number of defects.[71,72] Nitrogen doping of biomass is the pioneer route to boost MA_s materials.[72–79] Liu *et al.* synthesized an N-doped carbon microtubes/reduced graphene oxide (N-BCMT/RGO) composite aerogel to generate biomass from *Platanus acerifolia* fruit; an efficient bandwidth of 8.36 GHz and a maximum reflection loss of −55.45 dB were documented.[80] Moreover, they produced a vacancies-engineered and heteroatoms-regulated N-doped porous carbon aerogel (NPCA) synthesized by a gelatin-based process of organic polymer aerogel. The aerogel showed a reflection loss of −61.7 dB with a thickness of 2.6 mm and the efficient bandwidth of 11.7 GHz at a thickness range from 1 mm to 4 mm.[81] The retained porous structure and established defects in biomass-derived carbonaceous structures increase the specific surface area by extending the propagation field for EM waves but also by providing opportunities to generate multiple reflections and scatterings.[59,65,82–91] *In situ* polymerization and a reductive process of biomass by developing π-conjugated primary chains amplifies electronic properties by ''electron hopping'' and electron migration.[39,63,85,92–97]

We investigated the philosophy of nitrogen doping/exhausting and defects of peanut shells pyrolyzed in an N_2 environment in MAs. C, N, and O atoms. The elimination and doping of nitrogen in peanut shells was done with HCl, $NaNO_2$, and urea. Meanwhile, the bio-waste was defected by KOH using pyrolysis, heat treatment, ultrasound, and ball milling. By introducing vacancies and heteroatoms, the microwave-absorbing performance was tuned. A microwave-absorbing medium and interfacial polarization have pivotal roles in improving microwave-absorption characteristics by establishing and ameliorating microwave-absorbing mechanisms, including dipole and interfacial polarization. PMMA by development of electrostatic interactions, originating from esoteric functional groups, confined the agglomeration of guest molecules and augmented filler dispersion; moreover, functional groups established and improved dipole polarization and charge transition. In particular, the *in situ* polymerization of MMA monomers elevated the heterogeneous interfaces in the final product. In general, the unique physiochemical properties of PMMA enhanced the practical application of the fabricated composites.

2. Experimental

2.1. Materials

Peanut shells (PS) were purchased from a local confectionery in Tehran province, Iran. They were washed with ethanol and distilled water several times and then dried at 70 °C for 24 h in an oven. Hydrochloric acid (HCl, 37%, 6 M), potassium hydroxide (KOH), sodium nitrite ($NaNO_2$, 97.0%), urea (U), methyl methacrylate (MMA), benzoyl peroxide (BPO), and toluene were purchased from MilliporeSigma. All substrates were commercially available and used without further purification except MMA, which was dried by calcium chloride and toluene, and was distilled before application.

2.2. Preparation of carbonized peanut shells (C-PS)

In order to assess the impact of N-doping and porosity, the PS was selected as an affordable and sustainable carbon-based structure. PS were washed several times with ethanol and distilled water, dried at 70 °C for 24 h, and thoroughly cleaned using ultrasonic waves. The dried PS were powdered by ball milling at 40 rpm for 12 min. Subsequently, the as-prepared sample was carbonized at 750 °C for 3 h under an N_2 atmosphere.

2.3. Preparation of carbonized peanut shells/urea (C-PS/U)

Different laboratory conditions were considered to investigate the influence of nitrogen content on microwave-absorbing characteristics. The nitrogen ratio in the final carbonized structure was increased using urea (U) as a substrate. Urea

was used as a dopant. PS were rinsed with ethanol and distilled water several times and then dried at 70 °C for 24 h in an oven. Firstly, 1 g of PS was finely powdered by ball milling at 40 rpm for 6 min. Subsequently, the milled sample was doped with 0.038 g of U by ball milling at 40 rpm for another 6 min. Next, the component was subjected to a tubular furnace at 750 °C for 3 h in a nitrogen atmosphere to carbonize the bio-inspired structure.

2.4. Preparation of carbonized peanut shells/KOH/urea-1(C-PS/K/U-1)

Two scenarios (heat treatment by reflux and milling) were applied to compare the defect influence on the microwave-absorbing features using KOH as an activating agent. The defected nitrogen-doped biomass-derived material was synthesized by tuning the carbonization sequence of PS, KOH (K), and urea (U) at a constant mass ratio of 1 : 0.5 : 0.038.

After the same rinsing process, the PS were etched with 0.5 g of KOH by ball milling with a frequency of 40 rpm for 6 min. After that, the defected sample was washed with distilled water several times to reach neutral pH and dried for 24 h at ambient temperature. Next, the porous sample was reacted with urea as described above. Then, the B-PS/K/U-1 sample was pyrolyzed in the same conditions as before.

2.5. Preparation of carbonized peanut shells/KOH/urea-2(C-PS/K/U-2)

In order to prepare peanut shells/KOH/urea-2 (C-PS/K/U-2), all the aforementioned steps employed to synthesize B-PS/K/U-1 were similarly repeated. The only difference was that the PS were etched with 0.5 g of KOH by refluxing for 24 h at 100 °C instead of ball milling.

2.6. Elimination of nitrogen heteroatoms from the biomass-derived structure (N-D-C-PS)

A PS has amide functional groups in its chemical structure. In this step, amide species were hydrolyzed with HCl solvent. After breaking the C–N bond, nitrogen would be eliminated with HCl solvent and $NaNO_2$. The obtained sample was entitled "N-D-C-PS".

Initially, PS were washed and powdered by ball milling at 40 rpm for 12 min. Then, PS powder was dispersed in 25 mL of HCl (6 M). The suspension was transferred to a Teflon™ container of an industrial microwave and afterward underwent heating at 70 °C with power of 400 W for 15 min. Eventually, the hydrolyzed sample was washed with distilled water several times to reach a neutral pH. The hydrolyzed sample was suspended in 25 mL of HCl (6 M). The solution was transferred to a 250-mL beaker, cooled in an ice bath, and put under a ventilator. $NaNO_2$ (0.1 g) was added to the solution. A nitrogen-elimination reaction was detectable when brown gas had been exhausted. Subsequently, for complete removal of nitrogen-containing functional groups, the beaker was placed in an ultrasonic bath for 10 min. Afterwards, the hydrolyzed sample was washed with distilled water several times to reach a neutral pH and dried at room temperature for 24 h. The product was pyrolyzed at 750 °C for 3 h in a tubular furnace filled with a nitrogen atmosphere.

2.7. Fabrication of poly(methyl methacrylate)-based microwave-absorbing films

Polymerization was done by tuning the sequence of reinforced samples obtained in each step. Toluene, BPO, MMA, and tailored specimens, as the solvent, initiator, monomer, and microwave absorbing filler, respectively, were applied at a constant mass ratio of 4.3 : 0.5 : 4.7 : 0.2. An *in situ* polymerization procedure was conducted to fabricate PMMA-based microwave-absorbing architectures. As a result, 0.1 g of the architected samples were separately dispersed in 2.5 mL of toluene using an ultrasonic bath for 1 h and loaded in 2.5 ml of MMA. Following that, 0.25 g of BPO was added in a 50-ml round-bottom flask, substrates were added, and mixed by an overhead stirrer. The composites were cured by refluxing at 110 °C for 3 h. Eventually, the architected absorbers were rinsed with ethanol and dried in a vacuum oven at 100 °C for 12 h (Fig. 1).

2.8. Characterization

Fourier-transform infrared (FTIR) spectroscopy was done on a Tensor 27 system. X-ray diffraction (XRD) patterns were obtained using a Dron-8 diffractometer under Cu Kα radiation (λ = 1.540 Å) from 5° to 80°. The surface features of samples were studied by Brunauer–Emmett–Teller (BET) and Barrett–Joyner–Halenda (BJH) methods using N_2 adsorption/desorption isotherms. A Shimadzu UV-160 instrument characterized UV-Vis diffuse reflection spectroscopy (DRS). The morphology of samples was revealed by field emission scanning electron microscopy (FE-SEM) using a using a MIRA III (Tescan) system. A two-port vector network analyzer (E8364A) from Agilent Technologies was employed to estimate the microwave-absorbing characteristics of samples. An ultrasonic bath (Elma) served 80 kHz and 100 W of ultrasonic waves.

3. Results and discussion

3.1. FT-IR spectroscopy and crystal characterization

FT-IR spectroscopy was employed to characterize the functional groups of N-D-C-PS, C-PS, C-PS/U, C-PS/K/U-1, and C-PS/K/U-2 (Fig. 2(a)). The absorption band at 1584 cm^{-1} was ascribed to the bending vibrations of N–H, and stretching vibration of C–O and C═O. The peak at 2920 cm^{-1} was related to the stretching vibrations of aliphatic C–H. The broadband peak at 3428 cm^{-1} indicated the stretching vibrations of N–H, and was overlapped by the stretching vibrations of the adsorbed water and remaining hydroxyl groups. In addition, the shoulder above 3700 cm^{-1} corresponded to free O–H.[98] These spectra testified that N-doping enhanced the intensity of the peaks attributed to nitrogen-containing functional groups. In particular, the strengthened peaks of KOH-etched samples suggested that, by widening the heterogeneous interfaces, the active positions were boosted to couple with nitrogen along the doping route. More interestingly, the hydrolysis of amide with HCl and elimination procedure of amine with $NaNO_2$ was confirmed by mitigation of the absorption-band intensity associated with C–N and N–H functional groups.

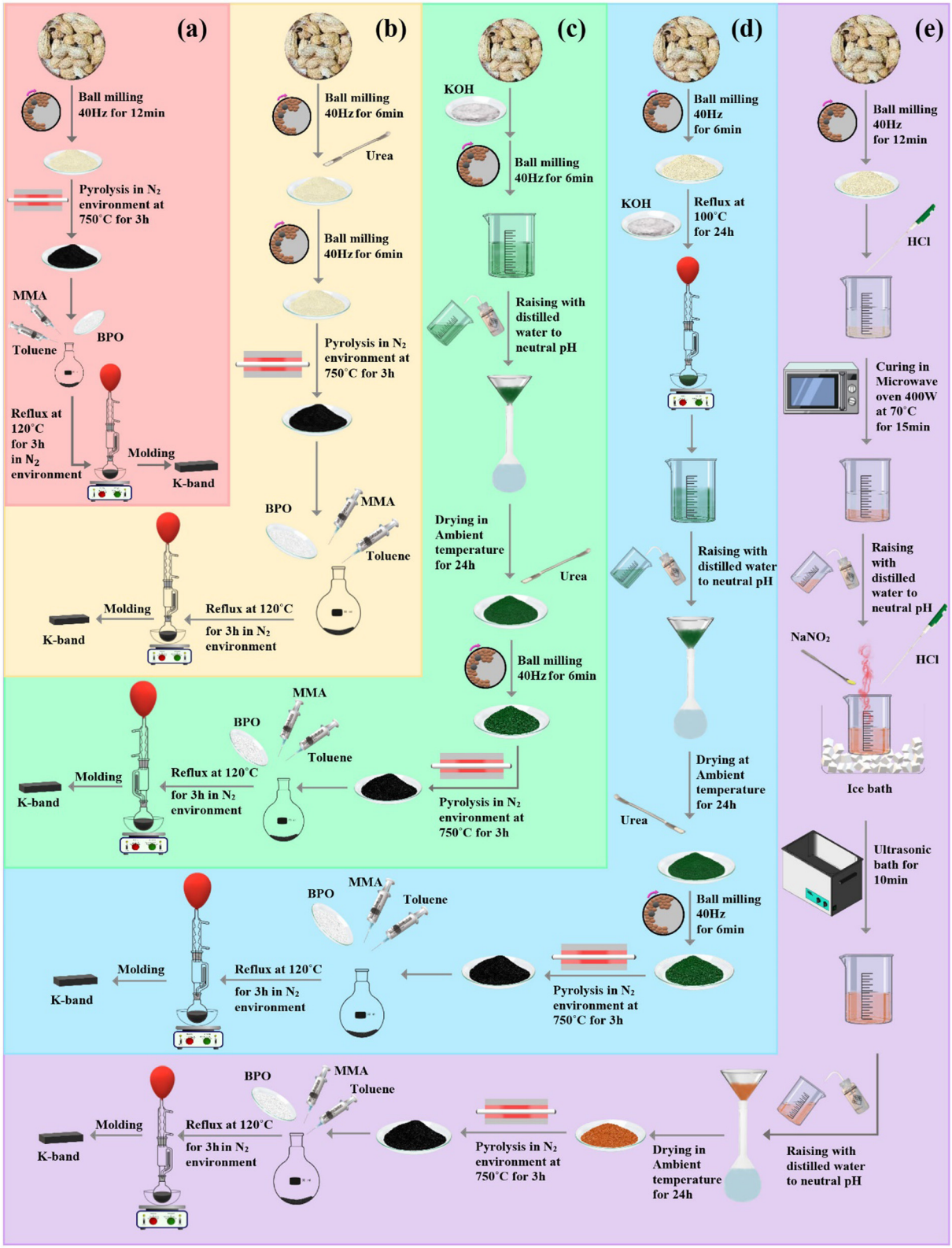

Fig. 1 Synthetic routes of C-PS (a), C-PS/U (b), C-PS/K/U-1 (c), C-PS/K/U-2 (d) and N-D-C-PS (e).

XRD patterns were used to study the crystal system of samples after carbonization. Fig. 2(b) depicts the XRD patterns of C-PS, C-PS/U, C-PS/K/U-1, C-PS/K/U-2, and N-D-C-PS samples. All XRD patterns of manufactured structures showed distinct peaks at 2θ = 22.5° and 43.5° corresponding to (200) and (100) crystal plans, respectively, governed by graphite.[34,35] The reductive

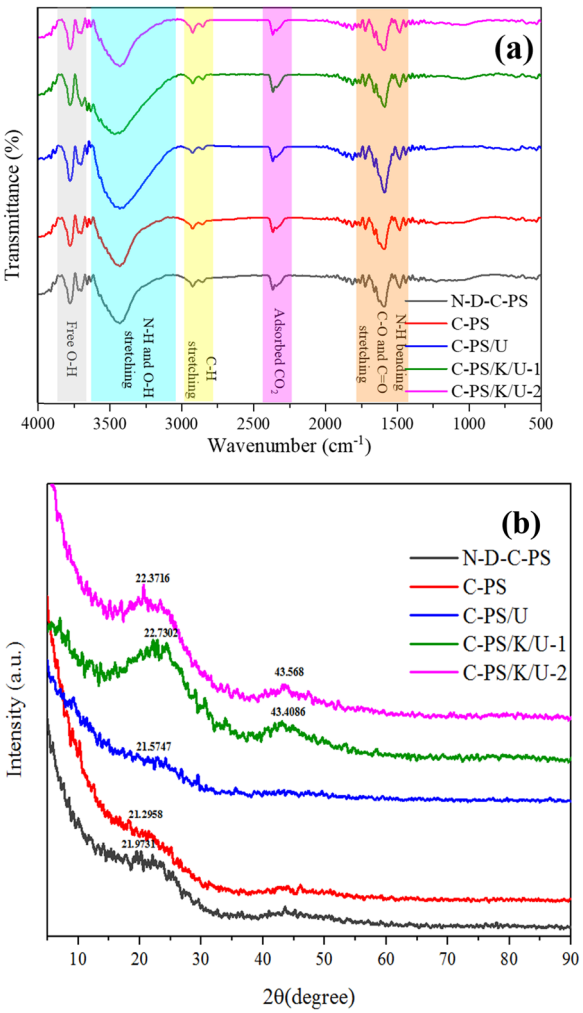

Fig. 2 FT-IR spectra (a) and XRD patterns (b) of samples.

process at high temperatures led to PS carbonization and established conjugated structures. Thus, the carbon plates were placed parallel or in the same direction, indicated by the formation of the amorphous crystal planes of graphite.[99] It is interesting to note that insertion of N atoms in the structure prevented creation of the conjugated structure, and the structure moved towards becoming amorphous. The spectra of C-PS/U showed that addition of an N atom in the structure led to a conjugated structure, and the structure moved towards becoming amorphous. We predicted that exhausting the N-containing groups would elicit more crystalline structures due to more π–π stacking and the development of conjugated structures. Evidently, by etching and increasing the number of heterogeneous interfaces, the oxygen-containing groups were facilely exhausted and generated more graphitized structures, as attested by C-PS/K/U-1 and C-PS/K/U-2 patterns. It should be noted that elimination of H_α in the presence of the base could ameliorate this scenario.[100,101]

3.2. FE-SEM micrographs and EDS

FE-SEM images of samples with diverse magnifications are displayed in Fig. 3. All of the pyrolysis structures had overall porous morphologies. Obviously, the N-D-C-PS sample hydrolyzed with HCl exhibited a reduced pore size, agglomerated morphology, and stacked particles stemming from the eliminated heteroatoms. The average pore size decreased in the C-PS/U sample after ball milling, and PS pores were partially blocked by depositing of nitrogen-containing atoms. N-doping elicited a smooth surface. Hence, the pore size increased upon KOH etching. As a result, the enhanced interfaces, rooted in KOH treatment, facilitated exhaustion of oxygen-containing functional groups and developed a rougher morphology, desirable for relaxation loss. These claims were confirmed by N_2 adsorption/desorption. Notably, the numerous nanosized bumps anchoring into the surfaces, burgeoned by exhausted heteroatoms and the catalytic effect of the remaining heteroatoms, enhanced interfacial polarization and microwave attenuation. Based on EDX, the weight percentage of carbon, nitrogen, and oxygen elements was presented in the pyrolyzed peanut shells (C-PS). After acid treatment and nitrogen removal, the nitrogen content was significantly decreased (N-D-C-PS). However, insertion of urea augmented the nitrogen content within the structure (C-PS/U) after carbonization. Furthermore, using KOH as an etching agent also boosted the nitrogen-containing structures compared with samples without a defect factor (C-PS/K/U-1, C-PS/K/U-2). These findings suggested that both urea and KOH had effective roles in manipulating the nitrogen content in the final product.

3.3. Surface characteristics

The porosity and specific surface area of the PS-derived structures were measured by N_2 adsorption/desorption isotherms. The specific surface area and pore size of samples are shown in Table S1 (ESI†). As shown in Fig. 4, at low relative pressure ($P/P_0 < 0.3$) of the nitrogen, absorption was low, which could have been related to a lack of porosity in the sample. C-PS/K/U-1, C-PS/K/U-2, and C-PS materials similarly followed the IV adsorption isotherm pattern with an H3-type hysteresis loop ($P/P_0 > 0.4$). C-PS/K/U-1 and C-PS/K/U-2 samples had the largest pore volume and specific surface due to the etching and defecting characteristics of KOH upon experimental treatments. However, C-PS had a lower specific surface area and pore volume compared with the samples modified with KOH. On the other hand, C-PS/U and N-D-C-PS samples exhibited the type-II isotherm, which indicated that the samples were without holes. Furthermore, the specific level was reduced in these samples. In the C-PS/U specimen, by loading urea, deposition of the urea derivate could make the surface characteristics disappear. Nonetheless, by removing nitrogen-containing functional groups from the N-D-C-PS sample, pyrolysis led to more π–π stacking because the main part of the structure consisted of C=C conjugated bonds, and placed together the crystal planes of graphite at high temperatures. Consequently, the more defective structure, rougher morphology, presence and exhaustion of the heteroatoms from biomass interlayers led to a more specific surface area, which is desirable for polarization loss. More significantly, ball milling enriched the surface characteristics. The bare biomass-derived structure and N-doped architectures had nanoscale diameters required for multiple reflections, scattering, and relaxation loss (Table 1).

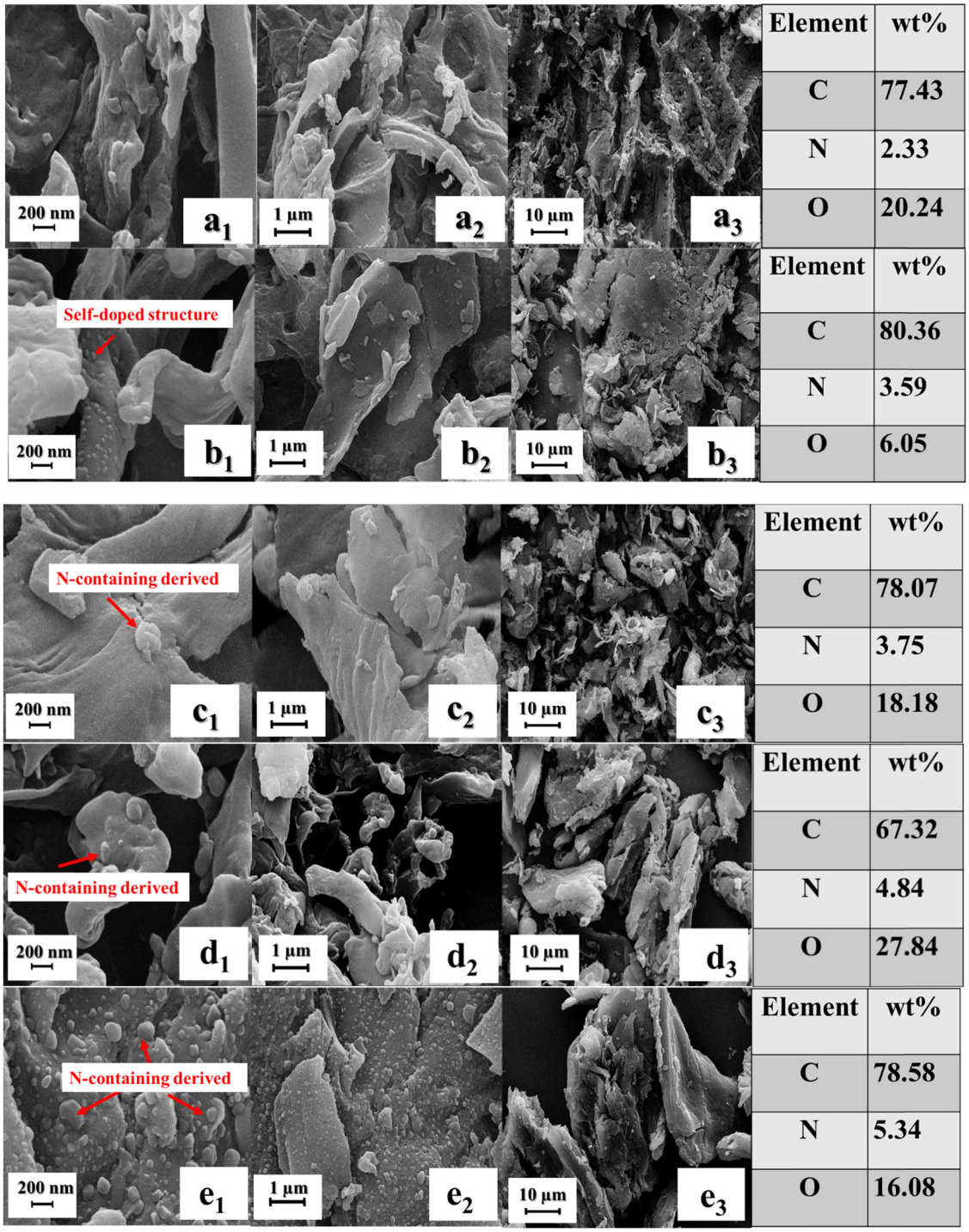

Fig. 3 FE-SEM micrographs and EDS of N-D-C-PS (a), C-PS (b), C-PS/U (c), C-PS/K/U-1 (d) and C-PS/K/U-2 (e) samples.

3.4. Optical performance

Light absorption from λ = 400 to 800 nm of the PS derivate was measured. Elimination of heteroatoms by facilitating charge transitions along conjugated structures and enhancement of heterogeneous interfaces by KOH treatment mitigated the absorption of visible light by amplifying light scattering and reflections. The Kubelka–Munk theory could be used to estimate the energy-band gaps of the bio-inspired samples. The distance between the highest occupied molecular orbital (HOMO) and lowest unoccupied molecular orbital (LUMO) defines the gap in energy bands. The n → π* (lone-pair electrons supplied by nitrogen and other heteroatoms) and π → π* charge transitions in the conjugated structure express the basic energy-band gap of the PS derivates. Introduction of N heteroatoms through the enrichment of electron-donating atoms resulted in structures that were softer and more polarizable. In contrast, etching

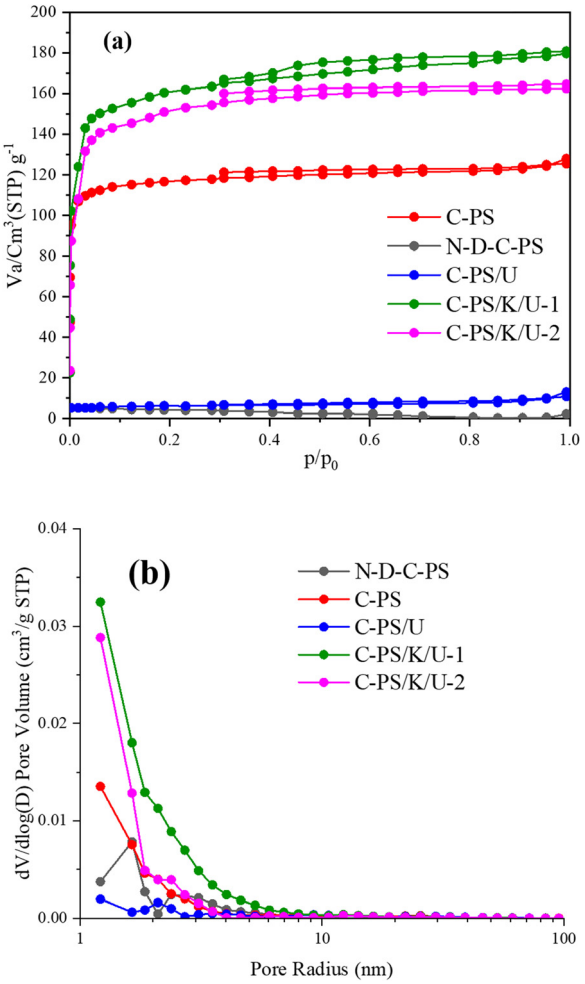

Fig. 4 N_2 adsorption/desorption isotherms (a) and pore-size distributions (b).

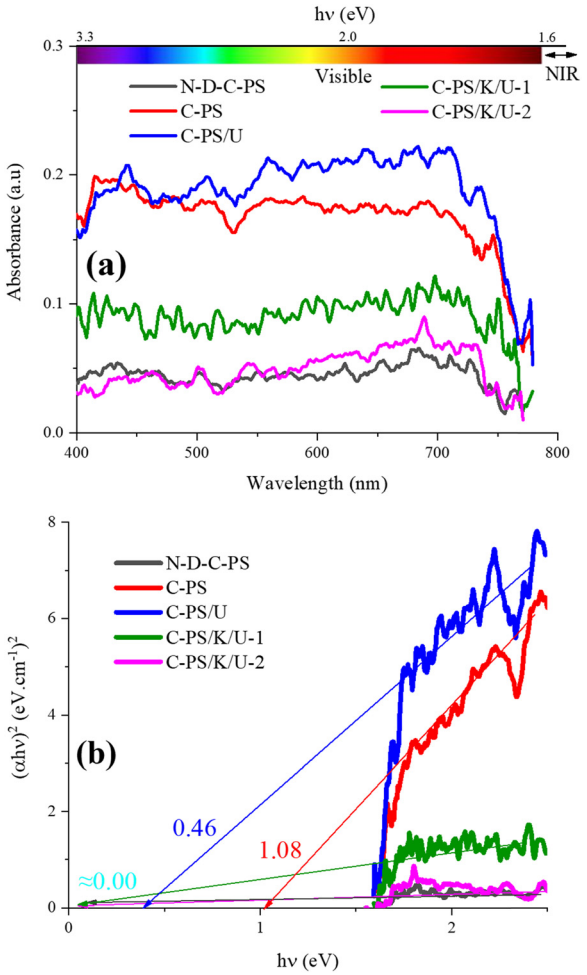

Fig. 5 Light absorption (a) and energy-band gap (b) of samples.

reduced the band gap to a value close to zero, primarily due to the increased porosity of the biomass. This enhanced porosity facilitated the removal of heteroatoms such as oxygen during pyrolysis. The optical properties of the samples are illustrated in Fig. 5.

3.5. Microwave absorbing/shielding performance

Fig. 6, 7, and Fig. S1 (ESI†) show reflection loss (RL), the curves of quarter-wavelength mechanism, as well as matching thicknesses of maximum RL and efficient bandwidth (EBW). C-PS/K/U-2/PMMA gained a RL of −81.34 dB at 25.61 GHz and an EBW of 8.50 GHz (RL ≤ −20 dB) with a thickness of 0.55 mm. The composite fabricated by PMMA using C-PS/U as a filler had an RL of −90.67 dB at 18.86 GHz and EBW of 7.52 GHz (RL≤ −10 dB) with a thickness of 1.55 mm. On the other hand, removal of heteroatoms led to a maximum RL of −92.38 dB at 23.32 GHz (RL≤ −20 dB) covering the entire K-band with a narrow thickness of 0.60 mm. Interestingly, the N-D-C-PS/PMMA sample covered all of the K-band (RL≤ −10 dB) from 0.4 to 0.9 mm. The maximum RL shifted to higher frequencies by a reduction in absorber thickness,

Table 1 Key properties of prepared peanut shell-derived samples

Sample name	Specific surface area ($m^2\ g^{-1}$)	Pore volume ($cm^3\ g^{-1}$)	Isotherm type	Additional notes
N-D-C-PS	0.10	—	Type II	Reduced surface characteristics due to the removal of nitrogen-containing functional groups.
C-PS	465.76	0.025	Type II	Lower specific surface area and pore volume compared to KOH-modified samples.
C-PS/U	4.24	0.012	Type II	Urea deposition affects surface characteristics, leading to reduced specific surface area.
C-PS/K/U-1	628.61	0.052	IV (H3 hysteresis loop)	Largest pore volume and specific surface area due to etching and defect characteristics of KOH.
C-PS/K/U-2	594.87	0.032	IV (H3 hysteresis loop)	Similar to C-PS/K/U-1, with comparable characteristics.

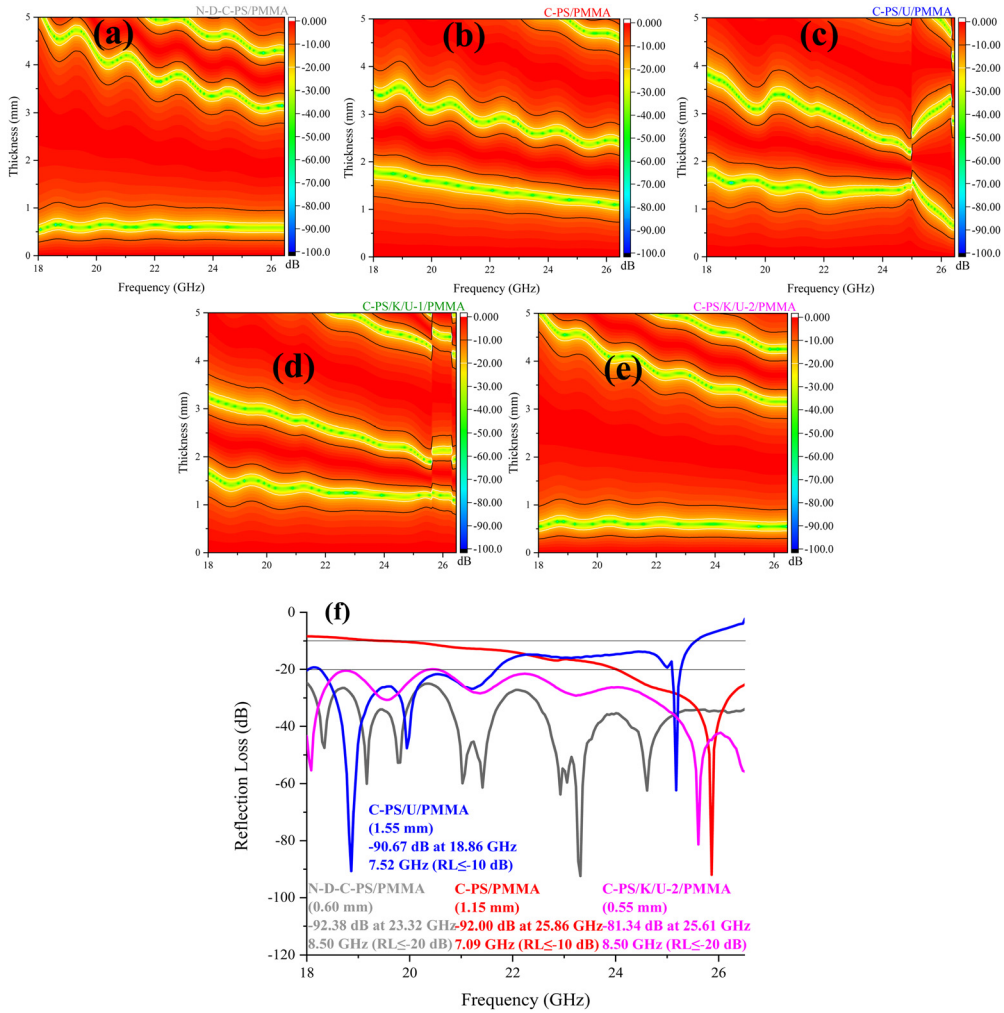

Fig. 6 2D plane views (a)–(e) and the best RL (f) of the phase- and morphology-modified samples at the K-band.

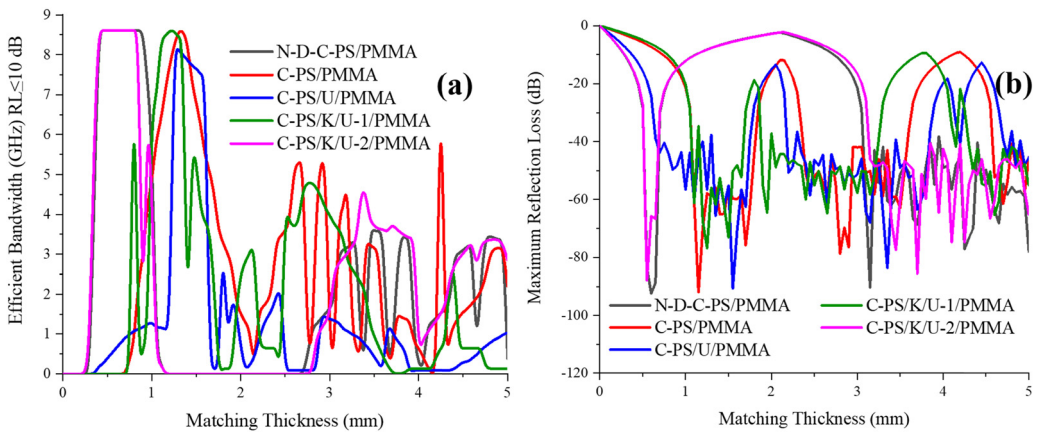

Fig. 7 Matching thickness associated with the highest result of efficient bandwidth (a) (RL ≤ 10 dB) and maximum RL (b) of PMMA-based composites.

governed by the quarter-wavelength mechanism. This mechanism is interpreted by incident waves being canceled by reflected waves if they are 180° out of phase from penetrated waves and the thickness of the absorber is an odd numeral of the propagated λ. Therefore, one of the notches observed in the RL curves was attributed to the above-mentioned mechanism.

Fig. 8 presents the real and imaginary parts of permittivity (ε' and ε'') and permeability (μ' and μ'') attributed to the doping-

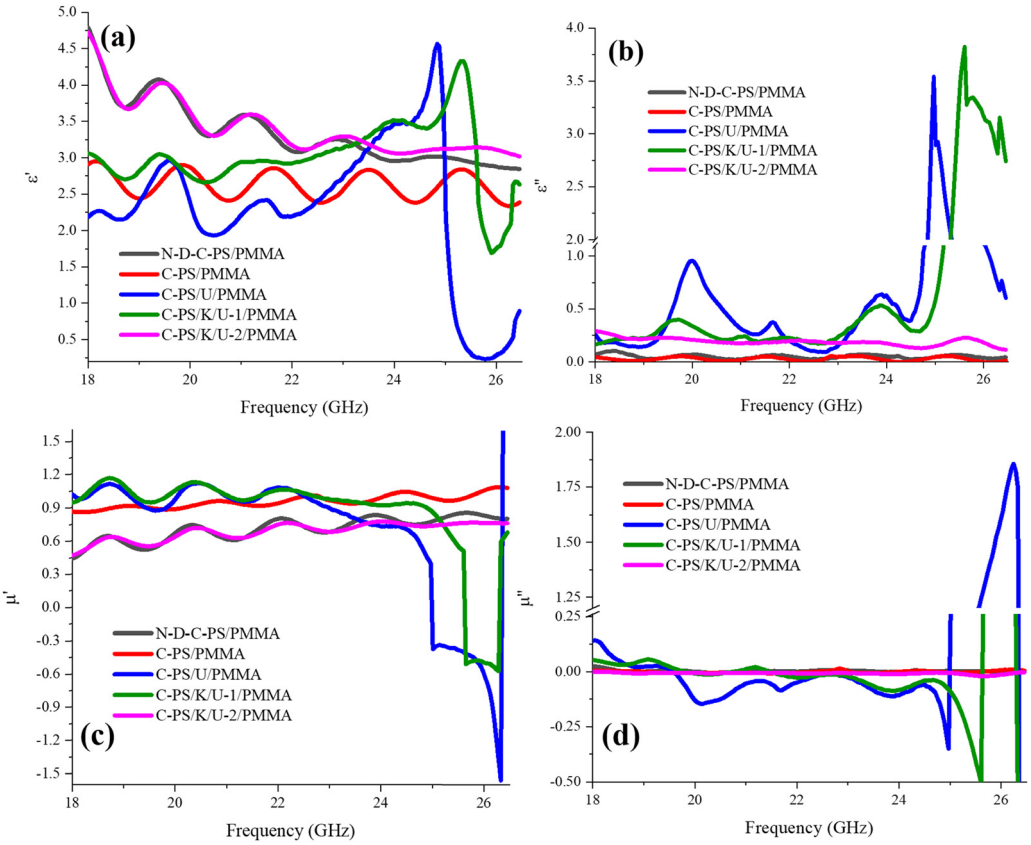

Fig. 8 Complex permittivity (a) and (b) and permeability curves (c) and (d) of doping-engineered composites at K-band frequencies.

engineered composites. The prime parts implied the storage ability and double-prime parts refer to the attenuation potential of the bio-inspired structures. Polarization–relaxation and electric conductivity create permittivity features, natural and exchange magnetic resonances, as well as properties aiding the permeability of eddy current constructs. ε′ is rooted in the polarizability of microwave-absorbing materials, and can be deduced by the Debye relaxation theory. Predictably, the KOH-treated samples as well as the nitrogen-eliminated specimen gained better polarization loss. This effect originated from the more porous structures, increased interfacial polarization, and more oxygen-containing functional groups amplifying polarization–relaxation, respectively. The observed bumps could be associated with the diverse types of polarization due to the presence of the various heteroatoms and types of etched morphologies. Relaxation and conductive loss comprise the imaginary part of permittivity. The π-to-π* charge transition along the conjugated structure after pyrolysis established the conductive loss. Results suggested that the denser structure (as given by the N_2 adsorption/desorption results) and loading of N-containing functional groups enriched the charge of conductive paths and augmented conductive loss, as attested by the C-PS/U/PMMA result. More interestingly, by N-doping, the conductive and relaxation loss of the biomass-derived materials were enhanced, generated from the overhanging bonds and enriched charges of the carbonaceous backbone. Permeability is derived from the eddy current and magnetic resonances (including natural and exchange resonances). It is notable that the tailored biowaste-derived structures were not magnetic material. Thus, the observed resonance peaks of permeability were essentially attributed to unpaired electrons (established by incomplete combustion during pyrolysis) as well as developed quasi-antennas by polarization and charge circuits inducing metamaterial features, magnetic fields, and permeability capabilities. In the raw peanut shell-derived structure (C-PS/U), the lack of surface modification resulted in even heteroatom self-doping. Fig. 8(a) indicates fluctuations in complex permittivity that deviate from conventional expectations. This behavior could be attributed to the unique morphological and compositional characteristics of C-PS/U and C-PS/K/U-1 samples. The nitrogen-doping process, involving the incorporation of urea, introduced complex interactions within the materials, thereby disrupting the typical alignment of electric dipoles. This disruption could lead to non-linear responses, resulting in the observed data, which may not conform to the normal rules of permittivity. Using urea as a nitrogen source promoted the formation of agglomerated derivates after milling, increasing the active surface area, surface plasmon resonance, exchange resonance, and quasi-antennas performance, which further amplified local polarization and dielectric fluctuations. In the case of C-PS/K/U-1, ball milling and chemical activation with potassium hydroxide introduced more functional groups and defects, which created active sites for magnetic interactions. This, along with the enlarged surface area, affected both polarization and spin distribution, contributing to

the fluctuations in dielectric and magnetic properties. For the C-PS/K/U-2 sample, reflux modification with potassium allowed for a controlled and even distribution of nitrogen and oxygen, leading to more consistent magnetic interactions with fewer fluctuations. This balanced structure allowed for consistent interactions with the EM field. The observed bumps in FESEM micrographs (b_1 and e_1), generated from the even distribution of nitrogen-containing derivates, mitigated the exchange resonance and quasi-antennas capability compared with those in C-PS/K/U-1 and C-PS/U. Therefore, the special morphology and agglomerated nitrogen-containing derivates, by boosting negative-charge accumulation under an alternating field, elevated dielectric resonances and metamaterial features. The negative values seen in the complex permeability (Fig. 8(c) and (d)) for C-PS/U and C-PS/K/U-1 samples could be explained by reverse polarization. In these materials, electric dipoles respond in an unconventional manner under the influence of an applied electric field. Instead of aligning with the field, dipoles may rotate or shift, causing positive and negative charges to move in opposing directions. This behavior resembles exchange resonance and can result in the generation of internal electric fields that counteract the external field, leading to negative permittivity and permeability. In the C-PS/U sample, the incorporation of nitrogen-containing functional groups could lead to fluctuations in dielectric properties. These functional groups disrupt conventional dipole alignment and can induce internal electric fields that may have contributed to the observed negative values. This enhancement of reactivity may amplify the effects of dipole movement, further contributing to the unusual behavior in permittivity data. The C-PS/K/U-1 sample, modified by KOH treatment, exhibited enhanced porosity and surface area. This modification promoted interfacial polarization and localized electric-field effects, which could exacerbate reverse polarization. The presence of defects and increased number of active sites for charge accumulation can lead to more pronounced fluctuations in dielectric and magnetic properties, further contributing to the observed negative values. Both samples demonstrated quasi-antenna characteristics, where they absorb EM waves but also radiate secondary EM fields due to displacement resonance. This dual functionality can lead to unexpected interactions that manifest as negative values in permittivity and permeability.

The attenuation constant (α), impedance matching (Z), eddy current (C_0), and Cole–Cole plot are illustrated in Fig. 9. The attenuation constant clarifies the absorber capacity for energy conversion, modulated by real and imaginary parts of dielectric and magnetic features. Doping and KOH treatment enhanced the energy-conversion properties of samples owing to the elevated relaxation loss, emerging secondary fields, conductive loss, as well as multiple reflection and scattering. The matched permittivity and permeability improved the ohmic resistance, thereby facilitating penetration of the incident waves into the absorbing medium. Impedance matching examines the absorber susceptibly to propagation of emitted waves. The closer Z is to 1 demonstrates the higher EM waves inputted from the

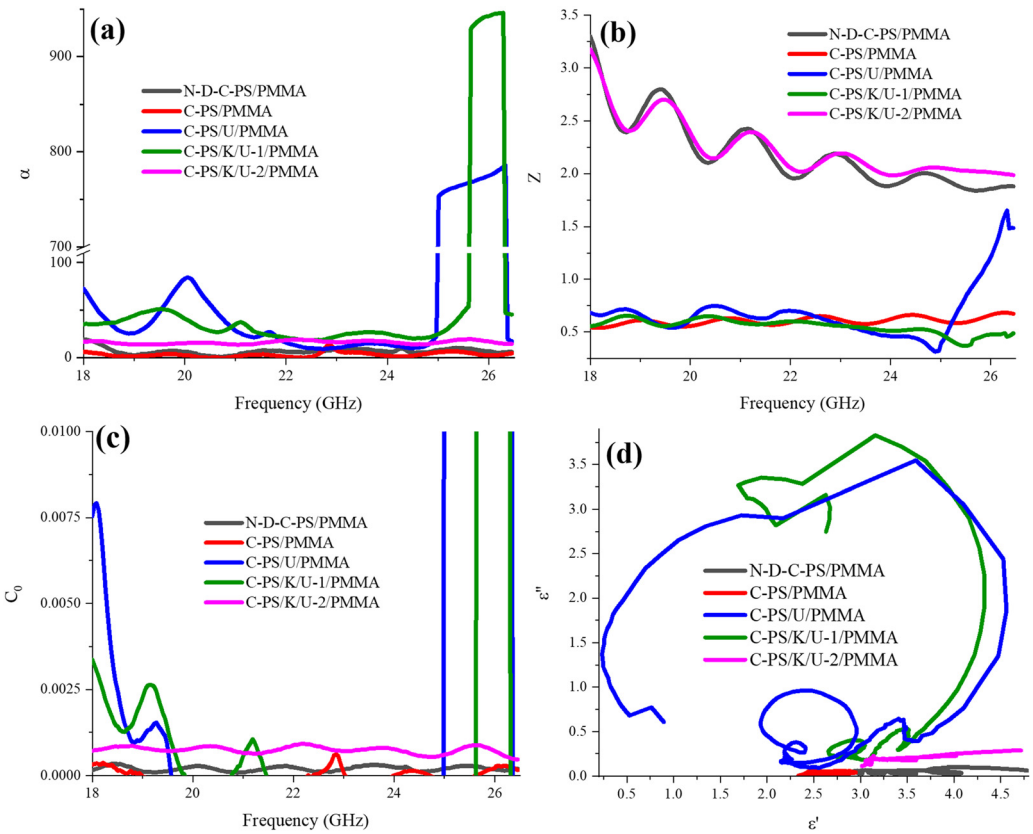

Fig. 9 α (a), Z (b), C_0 (c) and Cole–Cole plot (d) of architected samples at K-band frequencies.

absorber threshold, adjusted by manipulation of the heteroatoms and morphology. A constructive compromise between the α and Z suggests a remarkable RL. The constant eddy-current curve testified to greater loss of eddy current. These results suggested that elimination of N atoms and refluxing before N-doping strengthened the loss of eddy current. The polarization types and intensities were assessed by drawing ε' *versus* ε'', known as the Cole–Cole plot. Each established circular arc refers to one type of polarization when the first point and end point are placed in real parts and the center is below the arc.[102] The emerging semicircles suggested that milling and N-doping promoted polarization loss. However, refluxing before N-doping deteriorated the relaxation loss, which could be generated from the diminished electrophilic sites to nucleophilic attack of nitrogen along the reductive procedure by KOH. The depressed arcs and straight curves confirmed the conductive-loss ability of the absorbers. On the one hand, PMMA, due to the presence of esoteric functional groups and, on the other hand, the development of electrostatic interactions owing to its lone-pair electrons on their oxygen-containing groups and π^* (C═O), amplified the dipole polarization.

Humans are covered by harmful non-visible EM waves. Using technologies that apply/produce microwaves is inescapable during life. Hence, refining the hazardous waves simultaneously to maintain accessibility to modern devices is vital. Herein, engineered N-doping and etching by urea, milling, KOH, and reflux were applied to design moderate shielding composites. Notably, PMMA as a practical polymeric matrix, was fabricated using an *in situ* polymerization method.

Absorption of EM waves and shielding mechanisms are crucial for mitigating harmful waves. Both mechanisms rely on the dielectric and conductive properties of materials for efficient interaction with EM waves. In both mechanisms, EM energy is dissipated—through heat in absorption and through reflection, refraction, or absorption in shielding. Absorption reduces EM-wave intensity by converting it to heat, while shielding blocks external fields to protect sensitive components. Absorption relies on dielectric and conductive losses to dissipate energy as heat, while shielding uses reflection and scattering to block EM waves from reaching protected areas. Absorption performance is measured by RL and the absorption coefficient, while shielding effectiveness (SE) quantifies how well a material reduces incoming EM field intensity.[20,21] Nonetheless, all of the mechanisms bringing EM dissipation dominated in both types of materials. The shielding characteristics, including total shielding performance ($SE_T = SE_A + SE_R$), absorption shielding (SE_A), reflection shielding parameter (SE_R), and SE_T based on a percentage (SE_T%) are exhibited in Fig. 10. A favorable structure for shielding from EM interference works based on absorption because greater reflection maintains pollution in the environment. Shielding structures fabricated by PMMA of thickness 2 mm demonstrated moderate shielding performance, and could be desirable for

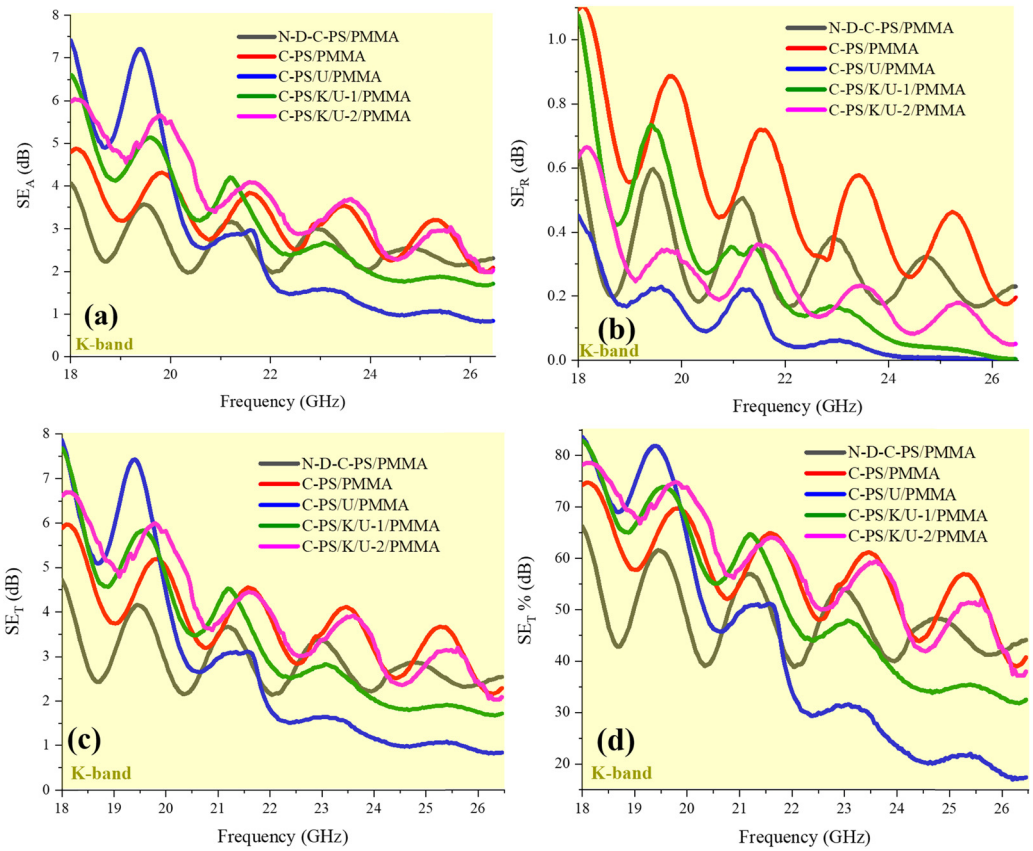

Fig. 10 SE_A (a), SE_R (b), SE_T (c), and percentage of SE_T (d) from 18 to 26.5 GHz.

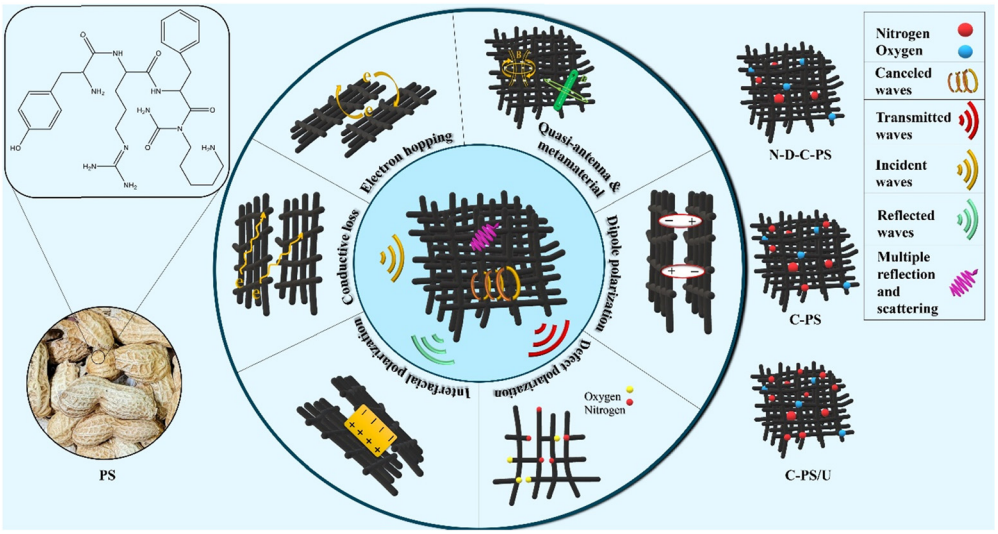

Fig. 11 Mechanisms eliciting microwave attenuation (schematic).

practical application using affordable and sustainable fillers. Absorption led to the shielding performance of samples, derived from the conductive, relaxation, and eddy-current loss as well as the permeability emerging by metamaterial properties and canceled waves, as established by multiple reflections and scattering. Equations estimating the microwave-absorbing characteristics and related parameters are presented in Tables S2 and S3 (ESI†). Fig. 11 is a schematic illustration of the microwave-absorbing mechanisms dominating in the microwave-absorbing medium fabricated by modified biomass and PMMA. We introduced a unique method for nitrogen-doping/eliminating and carbon structure-defects by HCl, $NaNO_2$, and urea during pyrolysis in an N_2 environment, which has not been fully explored before. By combining nitrogen-doping with structural defects developed *via* pyrolysis, ultrasound, heat treatment, and ball milling, the microwave-absorbing performance was boosted through dipole and interfacial polarization as well as natural and exchange resonances, canceled waves, and multiple reflections and scattering. Additionally, the *in situ* polymerization of MMA broadened heterogeneous interfaces, improved filler dispersion and microwave absorption by promoting dipole polarization and charge transfer, which distinguishes our approach from that of previous research.

4. Conclusions

We discussed the innovative routes to design microwave absorbing/shielding structures fabricated by affordable and sustainable substrates. PS were chosen as the polymeric backbone due to their porous structure, which is desirable for interfacial polarization. Then, ball milling and refluxing as well as KOH and urea engineered the N-doping ratio and porosity as the precursors. More significantly, nitrogen heteroatoms were eliminated to compare the influence of the presence of nitrogen atoms as a doping agent on microwave characteristics. Moreover, an *in situ* polymerization method served to prepare eventual composites using MMA as a monomer. It should be noted that the applied PMMA as a polymeric matrix promoted practical applications of the final products. Our results suggested that the applied novel processes regulated the specific surface area, morphology, optical performance, crystallinity, and microwave-absorbing features. The gained microwave absorption was rooted in dipole and interfacial polarization, multiple reflections and scattering, conductive loss, and established secondary fields tunable by the N-doping ratio and specific surface area. Our research sheds new light on the fabrication of affordable and "green" microwave-absorbing materials. Our data open new a vista for tuning their microwave-absorbing performance by a facile experimental procedure using cost-effective methods and precursors.

Data availability

The data supporting this article have been included as part of the ESI.†

Conflicts of interest

The authors declared they have no conflict of interest in connection with this research.

References

1 C. Ma, W.-T. Cao, W. Zhang, M.-G. Ma, W.-M. Sun, J. Zhang and F. Chen, *Chem. Eng. J.*, 2021, **403**, 126438.
2 P. Mou, J. Zhao, G. Wang, S. Shi, G. Wan, M. Zhou, Z. Deng, S. Teng and G. Wang, *Chem. Eng. J.*, 2022, **437**, 135285.
3 S. Yin, Y. Huang, C. Deng, Y. Jiao, W. Wu, F. Seidi and H. Xiao, *Compos. Sci. Technol.*, 2022, **218**, 109184.
4 M. Huang, L. Wang, B. Zhao, G. Chen and R. Che, *J. Mater. Sci. Technol.*, 2023, **138**, 149–156.
5 M. Zhou, J. Wang, S. Tan and G. Ji, *Mater. Today Phys.*, 2023, **31**, 100962.

6 L. Yao, W. Cao, J. Zhao, Q. Zheng, Y. Wang, S. Jiang, Q. Pan, J. Song, Y. Zhu and M. Cao, *J. Mater. Sci. Technol.*, 2022, **127**, 48–60.
7 Z. Zhou, X. Yang, D. Zhang, H. Zhang, J. Cheng, Y. Xiong, Z. Huang, H. Wang, P. Zhang and G. Zheng, *Adv. Compos. Hybrid Mater.*, 2022, **5**, 2317–2327.
8 Y.-S. Fang, J. Yuan, T.-T. Liu, Q.-Q. Wang, W.-Q. Cao and M.-S. Cao, *Carbon*, 2023, **201**, 371–380.
9 Y. Xie, S. Liu, K. Huang, B. Chen, P. Shi, Z. Chen, B. Liu, K. Liu, Z. Wu and K. Chen, *Adv. Mater.*, 2022, **34**, 2202982.
10 B. Zhao, X. Li, S. Zeng, R. Wang, L. Wang, R. Che, R. Zhang and C. B. Park, *ACS Appl. Mater. Interfaces*, 2020, **12**, 50793–50802.
11 H. Lv, Y. Li, Z. Jia, L. Wang, X. Guo, B. Zhao and R. Zhang, *Composites, Part B*, 2020, **196**, 108122.
12 J.-Q. Wang, Q. Zheng, W.-Q. Cao, H.-Z. Zhai and M.-S. Cao, *Adv. Compos. Hybrid Mater.*, 2024, **7**, 14.
13 R. Yu, L.-L. Liang, Y. Zhao and G. Ji, *J. Mater. Chem. A*, 2024, DOI: **10.1039/D3TA07615F**.
14 J. Cheng, Y. Jin, J. Zhao, Q. Jing, B. Gu, J. Wei, S. Yi, M. Li, W. Nie and Q. Qin, *Nano-Micro Lett.*, 2024, **16**, 1–40.
15 Y. Duan, Y. Cui, B. Zhang, G. Ma and W. Tongmin, *J. Alloys Compd.*, 2019, **773**, 194–201.
16 B. Mao, X. Xia, R. Qin, P. Li, G. Yang, H. Fu, H. Lv, X. Li, X. Jia and D. Xu, *J. Alloys Compd.*, 2023, **936**, 168314.
17 M. Sood and A. Rai, *Int. J. Commun. Syst.*, 2023, **36**, e5515.
18 S. Shelar, P. V. Kasambe and R. Kumbhare, Microstrip patch antenna with partial ground plane and parasitic patch for K band application in 5G, *2021 International Conference on Communication information and Computing Technology (ICCICT)*, IEEE, 2021.
19 J. Zhou, L. Liu, H. Shi, M. Zhu, X. Cheng, L. Ren, L. Ding, L.-M. Peng and Z. Zhang, *ACS Appl. Mater. Interfaces*, 2021, **13**, 37475–37482.
20 W. Q. Cao, M. Zhang and M. S. Cao, *Adv. Funct. Mater.*, 2024, 2410928.
21 H.-Z. Guan, J.-Y. Zong, M.-Q. Wang, H.-Z. Zhai, J. Yuan and M.-S. Cao, *Carbon*, 2024, **226**, 119239.
22 Y. Huo, D. Guo, J. Yang, Y. Chang, B. Wang, C. Mu, J. Xiang, A. Nie, K. Zhai and T. Xue, *ACS Appl. Electron. Mater.*, 2022, **4**, 2552–2560.
23 T. Li, D.-D. Zhi, Z.-H. Guo, J.-Z. Li, Y. Chen and F.-B. Meng, *Green Chem.*, 2022, **24**, 647–674.
24 Z. Li, W. Yang, B. Jiang, C. Wang, C. Zhang, N. Wu, C. Zhang, S. Du, S. Li and H. Bai, *ACS Appl. Mater. Interfaces*, 2023, **15**, 7578–7591.
25 L. Chang, Y.-Z. Wang, X.-C. Zhang, L. Li, H.-Z. Zhai and M.-S. Cao, *J. Mater. Sci. Technol.*, 2024, **174**, 176–187.
26 F. M. Idris, I. R. Ibrahim, F. N. Shafiee, H. Kaco and M. S. E. Shafie, *J. Adv. Res. Appl. Mech.*, 2024, **113**, 13–26.
27 W. Deng, T. Li, H. Li, J. Abdul, L. Liu, A. Dang, X. Liu, M. Duan and H. Wu, *Small*, 2024, 2309806.
28 X. Xie, Y. Wang, X. Sun, H. Wang, R. Yu, W. Du and H. Wu, *J. Mater. Sci. Technol.*, 2023, **133**, 1–11.
29 M. He, Q. Liao, Y. Zhou, Z. Song, Y. Wang, S. Feng, R. Xu, H. Peng, X. Chen and Y. Kang, *Langmuir*, 2022, **38**, 945–956.
30 Z. Yin, J. Wu, L. Liang, C. Kong, A. Pervikov, H. Shi and X. Li, *J. Alloys Compd.*, 2023, **966**, 171594.
31 L. Qin, B. Zeng, T. Qin, C. Li, C. Tang, S. Huang and L. Deng, *J. Mater. Sci.: Mater. Electron.*, 2023, **34**, 1478.
32 X. Wang, X. Huang, Z. Chen, X. Liao, C. Liu and B. Shi, *J. Mater. Chem. C*, 2015, **3**, 10146–10153.
33 Y. Akinay, B. Çolak, M. E. Turan, I. N. Akkuş, H. Ç. Kazici and A. O. Kizilçay, *Polym. Compos.*, 2022, **43**, 8784–8794.
34 Y. Akinay and I. N. Akkuş, *Ceram. Int.*, 2020, **46**, 17735–17740.
35 Y. Akinay, F. Hayat, M. Cakir and E. Akin, *Polym. Compos.*, 2018, **39**, 3418–3423.
36 Y. Akinay, F. Hayat, Y. Kanbur, H. Gokkaya and S. Polat, *Polym. Compos.*, 2018, **39**, E2143–E2148.
37 Y. Akinay and F. Hayat, *J. Compos. Mater.*, 2019, **53**, 593–601.
38 Y. Akinay and A. O. Kizilcay, *Polym. Compos.*, 2020, **41**, 227–232.
39 P. Chen, L.-K. Wang, G. Wang, M.-R. Gao, J. Ge, W.-J. Yuan, Y.-H. Shen, A.-J. Xie and S.-H. Yu, *Energy Environ. Sci.*, 2014, **7**, 4095–4103.
40 J. Ding, H. Wang, Z. Li, A. Kohandehghan, K. Cui, Z. Xu, B. Zahiri, X. Tan, E. M. Lotfabad and B. C. Olsen, *ACS Nano*, 2013, **7**, 11004–11015.
41 A. Fahimi, P. Fakharian, A. Mirakhan, A. Farahani, Z. Zhou, Y. Zhao and R. Peymanfar, *J. Mater. Chem. C*, 2024, DOI: **10.1039/D4TC01861C**.
42 P. J. Bora, M. J. HS, T. S. Kumar, S. Khasnabis and P. C. Ramamurthy, *Mater. Adv.*, 2021, **2**, 3715–3725.
43 Y. Jiang, Y. Chen, Y.-J. Liu and G.-X. Sui, *Chem. Eng. J.*, 2018, **337**, 522–531.
44 G. Wu, Y. Cheng, Z. Yang, Z. Jia, H. Wu, L. Yang, H. Li, P. Guo and H. Lv, *Chem. Eng. J.*, 2018, **333**, 519–528.
45 H. Lv, G. Ji, X. Liang, H. Zhang and Y. Du, *J. Mater. Chem. C*, 2015, **3**, 5056–5064.
46 W. Fu, W. Yang, C. Qian, Y. Fu and Y. Zhu, *ACS Appl. Nano Mater.*, 2023, **6**, 3728–3737.
47 W. Xu, W. Liao, H. Zhou, L. Wang, K. Huang, P. Li and J. Yu, *ACS Appl. Electron. Mater.*, 2024, **6**, 2759–2766.
48 Y. Wei, M. Zhang, C. Li, X. Wang, J. Zhang, S. Chen, J. Lin and R. Xiao, *J. Mater. Sci.*, 2024, 1–15.
49 F. Wu, Z. Liu, J. Wang, T. Shah, P. Liu, Q. Zhang and B. Zhang, *Chem. Eng. J.*, 2021, **422**, 130591.
50 E. Selseleh-Zakerin, A. Mirkhan, M. Shafiee, M. Alihoseini, M. Khani, B. Shokri, S. H. Tavassoli and R. Peymanfar, *Langmuir*, 2024, DOI: **10.1021/acs.langmuir.4c01046**.
51 M.-S. Cao, W.-L. Song, Z.-L. Hou, B. Wen and J. Yuan, *Carbon*, 2010, **48**, 788–796.
52 W. Deng, T. Li, H. Li, R. Niu, A. Dang, Y. Cheng and H. Wu, *Carbon*, 2023, **202**, 103–111.
53 X. Xiong, H. Zhang, H. Lv, L. Yang, G. Liang, J. Zhang, Y. Lai, H.-W. Cheng and R. Che, *Carbon*, 2024, 118834.
54 H. Luo, H. Rehman, X. Xia, J. Zheng, P. Li, Y. Li and J. Tong, *J. Alloys Compd.*, 2023, **968**, 172146.
55 Y. Liu, J. Lai and J.-F. Shi, *New Carbon Mater.*, 2020, **35**, 428–435.
56 Z. Chen, X. Sun, Z. Wang, Y. Zhu, C. Cao, J. Zhou and Y. Gao, *ACS Appl. Electron. Mater.*, 2022, **4**, 2424–2431.

57 L. Yuanyuan, Y. Jiuhong, Z. Yingying, Y. Chaoqun, W. Beibei and C. Haobo, *J. Mater. Sci.: Mater. Electron.*, 2023, **34**, 1892.
58 G. Fan, X. Song, X. Zhang, Q. Wang, Y. Tang and Y. Liu, *J. Alloys Compd.*, 2023, **969**, 172384.
59 Z. Wu, T. Huang, T. Li and L. Li, *Langmuir*, 2019, **35**, 3688–3693.
60 H. Guan, H. Wang, Y. Zhang, C. Dong, G. Chen, Y. Wang and J. Xie, *Appl. Surf. Sci.*, 2018, **447**, 261–268.
61 Q. Huang, C. Bao, Q. Wang, C. Dong and H. Guan, *Appl. Surf. Sci.*, 2020, **515**, 145974.
62 A. P. Alegaonkar, H. B. Baskey and P. S. Alegaonkar, *Mater. Adv.*, 2022, **3**, 1660–1672.
63 P. J. Bora, K. K. Khanum, R. K. Ramesh, K. Vinoy and P. C. Ramamurthy, *Mater. Adv.*, 2021, **2**, 3613–3619.
64 Z. Yao, S. Xu, X. Zhang, J. Yuan, C. Rong, Z. Xiong, X. Zhu, Y. Yu, H. Yu and S. Kang, *ACS Appl. Nano Mater.*, 2023, **6**, 1325–1338.
65 L. Guo, Q. An, Z.-Y. Xiao, S.-R. Zhai, W. Cai, H. Wang and Z. Li, *ACS Sustainable Chem. Eng.*, 2019, **7**, 19546–19555.
66 K. Ran, W. Wang, X. Hou, Y. Huang, Z. Zhang, D. He, Y. Fang, S. Wang, R. Zhao and W. Xue, *J. Alloys Compd.*, 2022, **924**, 166568.
67 Y. Li, X. Li, Q. Li, R. Zhang, Y. Zhao and J. Wang, *ACS Appl. Electron. Mater.*, 2022, **4**, 5941–5952.
68 Y. Karataş, T. Çetin, Y. Akinay and M. Gülcan, *J. Energy Inst.*, 2023, **109**, 101310.
69 B. Ulas, T. Cetin, M. Topuz and Y. Akinay, *Int. J. Hydrogen Energy*, 2024, **82**, 892–900.
70 B. Ulas, T. Çetin, Ş. Kaya, Y. Akinay and H. Kivrak, *Int. J. Hydrogen Energy*, 2024, **58**, 726–736.
71 P. Zhou, X. Wang, L. Wang, J. Zhang, Z. Song, X. Qiu, M. Yu and Q. Zhang, *J. Alloys Compd.*, 2019, **805**, 1071–1080.
72 K. Ghosh and S. K. Srivastava, *Langmuir*, 2021, **37**, 2213–2226.
73 J. Qiu, J. Liao, G. Wang, R. Du, N. Tsidaeva and W. Wang, *Chem. Eng. J.*, 2022, **443**, 136475.
74 T. Jia, X. Qi, L. Wang, J.-L. Yang, X. Gong, Y. Chen, Y. Qu, Q. Peng and W. Zhong, *Carbon*, 2023, **206**, 364–374.
75 S. Li, T. Xie, L. Ma, Z. Lei, N. Huang, H. Song, Y. Feng, B. Li, Y. Cui and L. Liu, *Carbon*, 2023, **213**, 118302.
76 L. Guo, Q.-D. An, Z.-Y. Xiao, S.-R. Zhai and L. Cui, *ACS Sustainable Chem. Eng.*, 2019, **7**, 9237–9248.
77 H. Tang, X. Li, K. Jin, Y. Shi, C. Wang, W. Guo, K. Tian, Y. Wang and H. Wang, *Appl. Surf. Sci.*, 2024, **653**, 159417.
78 H. Xing, Z. Chen, P. Fan, Z. Liu, P. Yang and X. Ji, *ACS Appl. Electron. Mater.*, 2023, **5**, 559–570.
79 H. Cai, Z. Lin, L. Gao, C. Feng and R. Tang, *J. Mater. Sci.*, 2024, **59**, 5371–5386.
80 P. Wu, Y. Feng, J. Xu, Z. Fang, Q. Liu and X. Kong, *Carbon*, 2023, **202**, 194–203.
81 P. Liu, S. Gao, C. Chen, F. Zhou, Z. Meng, Y. Huang and Y. Wang, *Carbon*, 2020, **169**, 276–287.
82 X. Xie, B. Wang, Y. Wang, C. Ni, X. Sun and W. Du, *Chem. Eng. J.*, 2022, **428**, 131160.
83 H. Guan, Q. Wang, X. Wu, J. Pang, Z. Jiang, G. Chen, C. Dong, L. Wang and C. Gong, *Composites, Part B*, 2021, **207**, 108562.
84 C. Lu, H. Geng, J. Ma, J. Zhao, R. Wang, Z. An and G. Tu, *ACS Appl. Nano Mater.*, 2023, **6**, 16778–16789.
85 T. Wei, X. Zhu, J. Xu, C. Kan and D. Shi, *Langmuir*, 2023, **39**, 890–898.
86 Y. Fan, Y. Li, Y. Yao, Y. Sun, B. Tong and J. Zhan, *Appl. Surf. Sci.*, 2020, **534**, 147510.
87 D.-d Wu, H.-x Zhang, Z.-y Wang, Y.-l Zhang and Y.-z Wang, *New Carbon Mater.*, 2023, **38**, 1035–1049.
88 J.-L. Wang, T. Yin, C. Zhang, W. Yang, B. Jiang, Y.-F. Li and C.-M. Xu, *New Carbon Mater.*, 2023, **38**, 875–886.
89 T. Zhu, R. Wang, J. Yang, C. Wang, W. Wang and W. Yang, *J. Mater. Sci.: Mater. Electron.*, 2023, **34**, 2149.
90 T. Bai, Y. Guo, H. Liu, G. Song, D. Zhang, Y. Wang, L. Mi, Z. Guo, C. Liu and C. Shen, *J. Mater. Chem. C*, 2020, **8**, 5191–5201.
91 X. Li, M. Cao, X. Pang, J. Hu and X. Yang, *J. Mater. Chem. C*, 2021, **9**, 1649–1656.
92 Y. Wang, Y. Du, P. Xu, R. Qiang and X. Han, *Polymers*, 2017, **9**, 29.
93 N. Velhal, N. Patil, G. Kulkarni, S. Shinde, N. Valekar, H. Barshilia and V. Puri, *J. Alloys Compd.*, 2019, **777**, 627–637.
94 H. Jia, H. Xing, X. Ji and S. Gao, *Appl. Surf. Sci.*, 2021, **537**, 147857.
95 H. Lv, Z. Yang, H. Xu, L. Wang and R. Wu, *Adv. Funct. Mater.*, 2020, **30**, 1907251.
96 S. Guo, D. Wang, X. Liu, J. Qin, C. Liu, J. Xu and J. Wang, *J. Mater. Sci.: Mater. Electron.*, 2024, **35**, 333.
97 E. He, T. Yan, X. Ye, Q. Gao, C. Yang, P. Yang, Y. Ye and H. Wu, *J. Mater. Sci.*, 2023, **58**, 11647–11665.
98 A. A. Kasani, H. G. Gilani and B. G. Choobar, *Groundw. Sustain. Dev.*, 2020, **11**, 100404.
99 J. Liang, W. Yang, A. C. Y. Yuen, H. Long, S. Qiu, I. M. De Cachinho Cordeiro, W. Wang, T. B. Y. Chen, Y. Hu and G. H. Yeoh, *Molecules*, 2021, **26**, 6662.
100 G. Shi, C. Liu, G. Wang, X. Chen, L. Li, X. Jiang, P. Zhang, Y. Dong, S. Jia and H. Tian, *Ionics*, 2019, **25**, 1805–1812.
101 S. Kohzadi, N. Marzban, Y. Zandsalimi, K. Godini, N. Amini, S. H. Puttaiah, S.-M. Lee, S. Zandi, R. Ebrahimi and A. Maleki, *Heliyon*, 2023, **9**, DOI: 10.1016/j.jclepro.2023.140409.
102 K. S. Cole and R. H. Cole, *J. Chem. Phys.*, 1941, **9**, 341–351.